Measurement of emission-angle anisotropy via long-range angular correlations with high-pThadrons in d+Au and p+p collisions at √sNN=200 GeV

(PHENIX Collaboration) Adare, A.; ...; Makek, Mihael; ...; Zou, L.

Measurement of emission-angle anisotropy via long-range angular correlations with high-p_T hadrons in d + Au and p + p collisions at $\sqrt{s_{NN}} = 200$ GeV

A. Adare,[13] C. Aidala,[45,46] N. N. Ajitanand,[66,*] Y. Akiba,[60,61,†] H. Al-Bataineh,[54] J. Alexander,[66] M. Alfred,[25] A. Angerami,[14] K. Aoki,[33,36,60] N. Apadula,[30,67] Y. Aramaki,[12,60] E. T. Atomssa,[37] R. Averbeck,[67] T. C. Awes,[56] B. Azmoun,[7] V. Babintsev,[26] A. Bagoly,[18] M. Bai,[6] G. Baksay,[21] L. Baksay,[21] K. N. Barish,[8] B. Bassalleck,[53] A. T. Basye,[1] S. Bathe,[5,8,61] V. Baublis,[59] C. Baumann,[47] A. Bazilevsky,[7] S. Belikov,[7,*] R. Belmont,[13,72] R. Bennett,[67] A. Berdnikov,[63] Y. Berdnikov,[63] J. H. Bhom,[76] D. S. Blau,[35,52] M. Boer,[40] J. S. Bok,[54,76] K. Boyle,[61,67] M. L. Brooks,[40] J. Bryslawskyj,[5,8] H. Buesching,[7] V. Bumazhnov,[26] G. Bunce,[7,61] S. Butsyk,[40] S. Campbell,[14,67] V. Canoa Roman,[67] A. Caringi,[48] C.-H. Chen,[61,67] C. Y. Chi,[14] M. Chiu,[7] I. J. Choi,[27,76] J. B. Choi,[10,*] R. K. Choudhury,[4] P. Christiansen,[42] T. Chujo,[71] P. Chung,[66] O. Chvala,[8] V. Cianciolo,[56] Z. Citron,[67,74] B. A. Cole,[14] Z. Conesa del Valle,[37] M. Connors,[23,61,67] M. Csanád,[18] T. Csörgő,[19,75] T. Dahms,[67] S. Dairaku,[36,60] I. Danchev,[72] T. W. Danley,[55] K. Das,[22] A. Datta,[45] M. S. Daugherity,[1] G. David,[7,67] M. K. Dayananda,[23] K. DeBlasio,[53] K. Dehmelt,[67] A. Denisov,[26] A. Deshpande,[61,67] E. J. Desmond,[7] K. V. Dharmawardane,[54] O. Dietzsch,[64] A. Dion,[30,67] J. H. Do,[76] M. Donadelli,[64] L. D'Orazio,[44] O. Drapier,[37] A. Drees,[67] K. A. Drees,[6] J. M. Durham,[40,67] A. Durum,[26] D. Dutta,[4] S. Edwards,[22] Y. V. Efremenko,[56] F. Ellinghaus,[13] T. Engelmore,[14] A. Enokizono,[56,60,62] H. En'yo,[60,61] S. Esumi,[71] B. Fadem,[48] W. Fan,[67] N. Feege,[67] D. E. Fields,[53] M. Finger,[9] M. Finger, Jr.,[9] F. Fleuret,[37] S. L. Fokin,[35] Z. Fraenkel,[74,*] J. E. Frantz,[55,67] A. Franz,[7] A. D. Frawley,[22] K. Fujiwara,[60] Y. Fukao,[60] Y. Fukuda,[71] T. Fusayasu,[50] C. Gal,[67] P. Gallus,[15] P. Garg,[3,67] I. Garishvili,[39,69] H. Ge,[67] A. Glenn,[39] H. Gong,[67] M. Gonin,[37] Y. Goto,[60,61] R. Granier de Cassagnac,[37] N. Grau,[2,14] S. V. Greene,[72] G. Grim,[40] M. Grosse Perdekamp,[27] T. Gunji,[12] H.-Å. Gustafsson,[42,*] T. Hachiya,[61] J. S. Haggerty,[7] K. I. Hahn,[20] H. Hamagaki,[12] J. Hamblen,[69] R. Han,[58] S. Y. Han,[20] J. Hanks,[14,67] S. Hasegawa,[31] T. O. S. Haseler,[23] E. Haslum,[42] R. Hayano,[12] X. He,[23] M. Heffner,[39] T. K. Hemmick,[67] T. Hester,[8] J. C. Hill,[30] K. Hill,[13] A. Hodges,[23] M. Hohlmann,[21] W. Holzmann,[14] K. Homma,[24] B. Hong,[34] T. Horaguchi,[24] D. Hornback,[69] T. Hoshino,[24] N. Hotvedt,[30] J. Huang,[7] S. Huang,[72] T. Ichihara,[60,61] R. Ichimiya,[60] Y. Ikeda,[71] K. Imai,[31,36,60] J. Imrek,[17] M. Inaba,[71] D. Isenhower,[1] M. Ishihara,[60] M. Issah,[72] D. Ivanishchev,[59] Y. Iwanaga,[24] B. V. Jacak,[67] Z. Ji,[67] J. Jia,[7,66] X. Jiang,[40] J. Jin,[14] B. M. Johnson,[7,23] T. Jones,[1] K. S. Joo,[49] V. Jorjadze,[67] D. Jouan,[57] D. S. Jumper,[1,27] F. Kajihara,[12] J. Kamin,[67] J. H. Kang,[76] J. Kapustinsky,[40] K. Karatsu,[36,60] S. Karthas,[67] M. Kasai,[60,62] D. Kawall,[45,61] M. Kawashima,[60,62] A. V. Kazantsev,[35] T. Kempel,[30] V. Khachatryan,[67] A. Khanzadeev,[59] K. M. Kijima,[24] J. Kikuchi,[73] A. Kim,[20] B. I. Kim,[34] C. Kim,[8,34] D. J. Kim,[32] E.-J. Kim,[10] M. Kim,[65] M. H. Kim,[34] Y.-J. Kim,[27] D. Kincses,[18] E. Kinney,[13] Á. Kiss,[18] E. Kistenev,[7] D. Kleinjan,[8] T. Koblesky,[13] L. Kochenda,[59] B. Komkov,[59] M. Konno,[71] J. Koster,[27] D. Kotov,[59,63] A. Král,[15] A. Kravitz,[14] S. Kudo,[71] G. J. Kunde,[40] B. Kurgyis,[18] K. Kurita,[60,62] M. Kurosawa,[60,61] Y. Kwon,[76] G. S. Kyle,[54] R. Lacey,[66] Y. S. Lai,[14] J. G. Lajoie,[30] A. Lebedev,[30] D. M. Lee,[40] J. Lee,[20,68] K. B. Lee,[34] K. S. Lee,[34] S. H. Lee,[30] M. J. Leitch,[40] M. A. L. Leite,[64] Y. H. Leung,[67] N. A. Lewis,[46] X. Li,[11] X. Li,[40] P. Lichtenwalner,[48] P. Liebing,[61] S. H. Lim,[40,76] L. A. Linden Levy,[13] T. Liška,[15] H. Liu,[40] M. X. Liu,[40] S. Lökös,[18,19] B. Love,[72] D. Lynch,[7] C. F. Maguire,[72] Y. I. Makdisi,[6] M. Makek,[77] M. D. Malik,[53] V. I. Manko,[35] E. Mannel,[7,14] Y. Mao,[58,60] H. Masuda,[62] H. Masui,[71] F. Matathias,[14] M. McCumber,[40,67] P. L. McGaughey,[40] D. McGlinchey,[13,22,40] N. Means,[67] B. Meredith,[27] W. J. Metzger,[19] Y. Miake,[71] T. Mibe,[33] A. C. Mignerey,[44] D. E. Mihalik,[67] K. Miki,[60,71] A. Milov,[7,74] D. K. Mishra,[4] J. T. Mitchell,[7] G. Mitsuka,[61] A. K. Mohanty,[4] H. J. Moon,[49] T. Moon,[76] Y. Morino,[12] A. Morreale,[8] D. P. Morrison,[7] S. I. Morrow,[72] T. V. Moukhanova,[35] T. Murakami,[36,60] J. Murata,[60,62] K. Nagai,[70] S. Nagamiya,[33,60] K. Nagashima,[24] J. L. Nagle,[13] M. Naglis,[74] M. I. Nagy,[18,75] I. Nakagawa,[60,61] H. Nakagomi,[60,71] Y. Nakamiya,[24] K. R. Nakamura,[36,60] T. Nakamura,[60] K. Nakano,[60,70] S. Nam,[20] C. Nattrass,[69] J. Newby,[39] M. Nguyen,[67] M. Nihashi,[24] R. Nouicer,[7,61] T. Novák,[19,75] N. Novitzky,[32,67] A. S. Nyanin,[35] C. Oakley,[23] E. O'Brien,[7] S. X. Oda,[12] C. A. Ogilvie,[30] M. Oka,[71] K. Okada,[61] Y. Onuki,[60] J. D. Orjuela Koop,[13] J. D. Osborn,[46] A. Oskarsson,[42] M. Ouchida,[24,60] K. Ozawa,[12,33,71] R. Pak,[7] V. Pantuev,[28,67] V. Papavassiliou,[54] I. H. Park,[20,68] J. S. Park,[65] S. Park,[60,65,67] S. K. Park,[34] W. J. Park,[34] S. F. Pate,[54] M. Patel,[30] H. Pei,[30] J.-C. Peng,[27] W. Peng,[72] H. Pereira,[16] D. V. Perepelitsa,[7,13] G. D. N. Perera,[54] D. Yu. Peressounko,[35] C. E. PerezLara,[67] R. Petti,[7,67] C. Pinkenburg,[7] R. P. Pisani,[7] M. Proissl,[67] A. Pun,[55] M. L. Purschke,[7] H. Qu,[23] P. V. Radzevich,[63] J. Rak,[32] I. Ravinovich,[74] K. F. Read,[56,69] S. Rembeczki,[21] K. Reygers,[47] V. Riabov,[52,59] Y. Riabov,[59,63] E. Richardson,[44] D. Richford,[5] T. Rinn,[30] D. Roach,[72] G. Roche,[41,*] S. D. Rolnick,[8] M. Rosati,[30] C. A. Rosen,[13] S. S. E. Rosendahl,[42] Z. Rowan,[5] J. Runchey,[30] P. Ružička,[29] B. Sahlmueller,[47,67] N. Saito,[33] T. Sakaguchi,[7] K. Sakashita,[60,70] H. Sako,[31] V. Samsonov,[52,59] S. Sano,[12,73] M. Sarsour,[23] K. Sato,[71] S. Sato,[31,33] T. Sato,[71] S. Sawada,[33] B. K. Schmoll,[69] K. Sedgwick,[8] J. Seele,[13] R. Seidl,[27,60,61] A. Sen,[30,69] R. Seto,[8] A. Sexton,[44] D. Sharma,[67,74] I. Shein,[26] T.-A. Shibata,[60,70] K. Shigaki,[24] M. Shimomura,[30,51,71] K. Shoji,[36,60] P. Shukla,[4] A. Sickles,[7,27] C. L. Silva,[30,40] D. Silvermyr,[42,56] C. Silvestre,[16] K. S. Sim,[34] B. K. Singh,[3] C. P. Singh,[3] V. Singh,[3] M. J. Skoby,[46] M. Slunečka,[9] R. A. Soltz,[39] W. E. Sondheim,[40] S. P. Sorensen,[69] I. V. Sourikova,[7] P. W. Stankus,[56] E. Stenlund,[42] S. P. Stoll,[7] T. Sugitate,[24] A. Sukhanov,[7] J. Sziklai,[75] E. M. Takagui,[64] A. Takeda,[51] A. Taketani,[60,61] R. Tanabe,[71] Y. Tanaka,[50] S. Taneja,[67] K. Tanida,[31,36,60,61,65] M. J. Tannenbaum,[7] S. Tarafdar,[3,72] A. Taranenko,[52,66] G. Tarnai,[17] H. Themann,[67] D. Thomas,[1] T. L. Thomas,[53] R. Tieulent,[43] A. Timilsina,[30] M. Togawa,[61] A. Toia,[67] L. Tomášek,[29] H. Torii,[24] C. L. Towell,[1] R. S. Towell,[1] I. Tserruya,[74] Y. Tsuchimoto,[24]

Y. Ueda,[24] B. Ujvari,[17] C. Vale,[7] H. Valle,[72] H. W. van Hecke,[40] S. Vazquez-Carson,[13] E. Vazquez-Zambrano,[14] A. Veicht,[14,27] J. Velkovska,[72] R. Vértesi,[75] M. Virius,[15] V. Vrba,[15,29] E. Vznuzdaev,[59] X. R. Wang,[54,61] Z. Wang,[5] D. Watanabe,[24] K. Watanabe,[71] Y. Watanabe,[60,61] F. Wei,[30,54] R. Wei,[66] J. Wessels,[47] S. N. White,[7] D. Winter,[14] C. L. Woody,[7] R. M. Wright,[1] M. Wysocki,[13,56] C. Xu,[54] Q. Xu,[72] Y. L. Yamaguchi,[12,60,61,67] K. Yamaura,[24] R. Yang,[27] A. Yanovich,[26] P. Yin,[13] J. Ying,[23] S. Yokkaichi,[60,61] J. H. Yoo,[34] Z. You,[58] G. R. Young,[56] I. Younus,[38,53] H. Yu,[54] I. E. Yushmanov,[35] W. A. Zajc,[14] S. Zharko,[63] S. Zhou,[11] and L. Zou[8]

(PHENIX Collaboration)

[1]*Abilene Christian University, Abilene, Texas 79699, USA*
[2]*Department of Physics, Augustana University, Sioux Falls, South Dakota 57197, USA*
[3]*Department of Physics, Banaras Hindu University, Varanasi 221005, India*
[4]*Bhabha Atomic Research Centre, Bombay 400 085, India*
[5]*Baruch College, City University of New York, New York, New York, 10010 USA*
[6]*Collider-Accelerator Department, Brookhaven National Laboratory, Upton, New York 11973-5000, USA*
[7]*Physics Department, Brookhaven National Laboratory, Upton, New York 11973-5000, USA*
[8]*University of California–Riverside, Riverside, California 92521, USA*
[9]*Charles University, Ovocný trh 5, Praha 1, 116 36 Prague, Czech Republic*
[10]*Chonbuk National University, Jeonju 561-756, Korea*
[11]*Science and Technology on Nuclear Data Laboratory, China Institute of Atomic Energy, Beijing 102413, People's Republic of China*
[12]*Center for Nuclear Study, Graduate School of Science, University of Tokyo, 7-3-1 Hongo, Bunkyo, Tokyo 113-0033, Japan*
[13]*University of Colorado, Boulder, Colorado 80309, USA*
[14]*Columbia University, New York, New York 10027 and Nevis Laboratories, Irvington, New York 10533, USA*
[15]*Czech Technical University, Zikova 4, 166 36 Prague 6, Czech Republic*
[16]*Dapnia, CEA Saclay, F-91191, Gif-sur-Yvette, France*
[17]*Debrecen University, H-4010 Debrecen, Egyetem tér 1, Hungary*
[18]*ELTE, Eötvös Loránd University, H-1117 Budapest, Pázmány Péter sétány 1/A, Hungary*
[19]*Eszterházy Károly University, Károly Róbert Campus, H-3200 Gyöngyös, Mátrai út 36, Hungary*
[20]*Ewha Womans University, Seoul 120-750, Korea*
[21]*Florida Institute of Technology, Melbourne, Florida 32901, USA*
[22]*Florida State University, Tallahassee, Florida 32306, USA*
[23]*Georgia State University, Atlanta, Georgia 30303, USA*
[24]*Hiroshima University, Kagamiyama, Higashi-Hiroshima 739-8526, Japan*
[25]*Department of Physics and Astronomy, Howard University, Washington, DC 20059, USA*
[26]*IHEP Protvino, State Research Center of Russian Federation, Institute for High Energy Physics, Protvino 142281, Russia*
[27]*University of Illinois at Urbana-Champaign, Urbana, Illinois 61801, USA*
[28]*Institute for Nuclear Research of the Russian Academy of Sciences, Prospekt 60-letiya Oktyabrya 7a, Moscow 117312, Russia*
[29]*Institute of Physics, Academy of Sciences of the Czech Republic, Na Slovance 2, 182 21 Prague 8, Czech Republic*
[30]*Iowa State University, Ames, Iowa 50011, USA*
[31]*Advanced Science Research Center, Japan Atomic Energy Agency, 2-4 Shirakata Shirane, Tokai-mura, Naka-gun, Ibaraki-ken 319-1195, Japan*
[32]*Helsinki Institute of Physics and University of Jyväskylä, P.O. Box 35, FI-40014 Jyväskylä, Finland*
[33]*KEK, High Energy Accelerator Research Organization, Tsukuba, Ibaraki 305-0801, Japan*
[34]*Korea University, Seoul, 136-701, Korea*
[35]*National Research Center "Kurchatov Institute", Moscow 123098, Russia*
[36]*Kyoto University, Kyoto 606-8502, Japan*
[37]*Laboratoire Leprince-Ringuet, Ecole Polytechnique, CNRS-IN2P3, Route de Saclay, F-91128 Palaiseau, France*
[38]*Physics Department, Lahore University of Management Sciences, Lahore 54792, Pakistan*
[39]*Lawrence Livermore National Laboratory, Livermore, California 94550, USA*
[40]*Los Alamos National Laboratory, Los Alamos, New Mexico 87545, USA*
[41]*LPC, Université Blaise Pascal, CNRS-IN2P3, Clermont-Fd, 63177 Aubiere Cedex, France*
[42]*Department of Physics, Lund University, Box 118, SE-221 00 Lund, Sweden*
[43]*IPNL, CNRS/IN2P3, Université Lyon, Universit Lyon 1, F-69622 Villeurbanne, France*
[44]*University of Maryland, College Park, Maryland 20742, USA*
[45]*Department of Physics, University of Massachusetts, Amherst, Massachusetts 01003-9337, USA*
[46]*Department of Physics, University of Michigan, Ann Arbor, Michigan 48109-1040, USA*
[47]*Institut für Kernphysik, University of Muenster, D-48149 Muenster, Germany*
[48]*Muhlenberg College, Allentown, Pennsylvania 18104-5586, USA*
[49]*Myongji University, Yongin, Kyonggido 449-728, Korea*
[50]*Nagasaki Institute of Applied Science, Nagasaki-shi, Nagasaki 851-0193, Japan*

[51]*Nara Women's University, Kita-uoya Nishi-machi Nara 630-8506, Japan*
[52]*National Research Nuclear University, MEPhI, Moscow Engineering Physics Institute, Moscow 115409, Russia*
[53]*University of New Mexico, Albuquerque, New Mexico 87131, USA*
[54]*New Mexico State University, Las Cruces, New Mexico 88003, USA*
[55]*Department of Physics and Astronomy, Ohio University, Athens, Ohio 45701, USA*
[56]*Oak Ridge National Laboratory, Oak Ridge, Tennessee 37831, USA*
[57]*IPN-Orsay, Université Paris-Sud, CNRS/IN2P3, Université Paris-Saclay, BP1, F-91406 Orsay, France*
[58]*Peking University, Beijing 100871, People's Republic of China*
[59]*PNPI, Petersburg Nuclear Physics Institute, Gatchina, Leningrad Region 188300, Russia*
[60]*RIKEN Nishina Center for Accelerator-Based Science, Wako, Saitama 351-0198, Japan*
[61]*RIKEN BNL Research Center, Brookhaven National Laboratory, Upton, New York 11973-5000, USA*
[62]*Physics Department, Rikkyo University, 3-34-1 Nishi-Ikebukuro, Toshima, Tokyo 171-8501, Japan*
[63]*Saint Petersburg State Polytechnic University, St. Petersburg 195251, Russia*
[64]*Universidade de São Paulo, Instituto de Física, Caixa Postal 66318, São Paulo CEP05315-970, Brazil*
[65]*Department of Physics and Astronomy, Seoul National University, Seoul 151-742, Korea*
[66]*Chemistry Department, Stony Brook University, SUNY, Stony Brook, New York 11794-3400, USA*
[67]*Department of Physics and Astronomy, Stony Brook University, SUNY, Stony Brook, New York 11794-3800, USA*
[68]*Sungkyunkwan University, Suwon 440-746, Korea*
[69]*University of Tennessee, Knoxville, Tennessee 37996, USA*
[70]*Department of Physics, Tokyo Institute of Technology, Oh-okayama, Meguro, Tokyo 152-8551, Japan*
[71]*Tomonaga Center for the History of the Universe, University of Tsukuba, Tsukuba, Ibaraki 305, Japan*
[72]*Vanderbilt University, Nashville, Tennessee 37235, USA*
[73]*Waseda University, Advanced Research Institute for Science and Engineering, 17 Kikui-cho, Shinjuku-ku, Tokyo 162-0044, Japan*
[74]*Weizmann Institute, Rehovot 76100, Israel*
[75]*Institute for Particle and Nuclear Physics, Wigner Research Centre for Physics, Hungarian Academy of Sciences (Wigner RCP, RMKI) H-1525 Budapest 114, P.O. Box 49, Budapest, Hungary*
[76]*Yonsei University, IPAP, Seoul 120-749, Korea*
[77]*Department of Physics, Faculty of Science, University of Zagreb, Bijenička c. 32 HR-10002 Zagreb, Croatia*

(Received 27 November 2017; revised manuscript received 23 March 2018; published 26 July 2018)

We present measurements of two-particle angular correlations between high-transverse-momentum ($2 < p_T < 11$ GeV/c) π^0 observed at midrapidity ($|\eta| < 0.35$) and particles produced either at forward ($3.1 < \eta < 3.9$) or backward ($-3.7 < \eta < -3.1$) rapidity in $d+$Au and $p+p$ collisions at $\sqrt{s_{NN}} = 200$ GeV. The azimuthal angle correlations for particle pairs with this large rapidity gap in the Au-going direction exhibit a characteristic structure that persists up to $p_T \approx 6$ GeV/c and which strongly depends on collision centrality, which is a similar characteristic to the hydrodynamical particle flow in $A+A$ collisions. The structure is absent in the d-going direction as well as in $p+p$ collisions, in the transverse-momentum range studied. The results indicate that the structure is shifted in the Au-going direction toward more central collisions, similar to the charged-particle pseudorapidity distributions.

DOI: 10.1103/PhysRevC.98.014912

I. INTRODUCTION

Azimuthal anisotropy in the multiparticle production from high-energy nucleus-nucleus collisions has been the subject of a great deal of study. These final-state momentum anisotropies are believed to be the result of both spatial anisotropies in the initial geometry and hydrodynamic-like behavior in the subsequent evolution of the medium. The final-state patterns that can be modeled this way are thus often referred to as flow-like correlations, for which a central characteristic is that the majority of produced light-flavor hadrons will exhibit correlations with the initial collision geometry. The measurement of azimuthal correlations of particles with a large rapidity gap (e.g., $|\Delta\eta| > 3$) is particularly useful to extract the signal of the true flow contribution. The near-side enhancement of the long-range correlation function is often called a "ridge" structure, where the large relative pseudorapidity cut suppresses other sources of angular correlations, such as resonance decays or jet fragmentation, that are usually confined within $|\Delta\eta| \approx 3$.

Analysis of flow-like correlations with hydrodynamical models has provided strong evidence for the creation of the quark-gluon plasma (QGP) state in the high-energy collisions of large nuclei, such as Au+Au and Cu+Cu at the Relativistic

*Deceased.
†PHENIX Spokesperson: akiba@rcf.rhic.bnl.gov

Heavy Ion Collider (RHIC) and Pb+Pb at the Large Hadron Collider (LHC) [1,2]. Great interest was sparked when flow-like behavior was first observed in small collision systems, including high-multiplicity $p+p$ and $p+\mathrm{Pb}$ at the LHC [3–8] and $d+\mathrm{Au}$ at RHIC [9–11]. Previously, these systems had been regarded as control systems where only non-QGP effects would be present. Since then, similar flow-like observations have also been made in other small systems, including $p+\mathrm{Au}$ and $^3\mathrm{He}+\mathrm{Au}$. The debate continues over whether the QGP is actually being created in this class of collisions [12,13], and even at lower $\sqrt{s_{NN}}$ [14,15]. Possible explanations of these observations include hydrodynamics [16–19] and color-glass-condensate (CGC) models [20]. The hydrodynamic models include both initial and final state effects, while the CGC-motivated models are based mainly on physics present in the initial state. Interestingly, the kinetic transport model AMPT [21] also reproduces the observed flow structure fairly well [13–15]. Similarly to hydrodynamics, AMPT can translate the initial geometry into final-state momentum anisotropy, but via a very different mechanism, namely the anisotropic probability of partons to escape the partonic scattering stage [22].

The PHENIX experiment has previously measured azimuthal correlations in $d+\mathrm{Au}$ and $p+p$ between charged particles produced at midrapidity (pseudorapidity $|\eta| \approx 0$) and energy deposits in a forward calorimeter ($|\eta| \approx 3.5$) [10]. In those analyses, the reach in charged particle p_T was statistically limited to $p_T < 3.5$ GeV/c. Measurements of azimuthal anisotropy at low p_T are useful to study the collective behavior of the QGP medium. However, at high p_T, azimuthal anisotropy signals can no longer be attributed to the collective expansion of the bulk. Measurements in $p+\mathrm{Pb}$ at the LHC [7,23] have shown that v_2 decreases sharply in the range $4 \lesssim p_T \lesssim 8$ GeV/c, reaching a small near-constant value above that point. It has been suggested that this high-p_T behavior might originate from jet quenching. Therefore, the present paper extends the measurements of two-particle correlations at RHIC to this kinematic region where nonhydrodynamic effects dominate. We use the PHENIX high-energy photon trigger in the midrapidity region, and explore mid-forward(backward) correlations in $d+\mathrm{Au}$ and $p+p$ up to $p_T = 11$ GeV/c with identified π^0 at midrapidity.

In large collision systems, the appearance of a near-side enhancement in azimuthal two-particle correlations is considered a hallmark signature of QGP collectivity. Thus, early searches for collectivity in small collision systems focused on observing near-side enhancement. However, unlike in $A+A$ collisions, elementary processes cannot be neglected when analyzing small systems. Thus, even if collectivity exists, it may not be necessarily observed as a near-side enhancement because the ratio of quadrupole to dipole contributions is decreasing with multiplicity. This is particularly true for $p+p$ and peripheral $d+\mathrm{Au}$ collisions, as the "smallest" of the small systems considered in the present analysis. In light of this, the paper presents a wealth of data and attempts to characterize the shape of the two-particle correlation functions by investigating the behavior of the coefficients of the Fourier series fit, in relation to the appearance of a near-side enhancement.

In addition to measuring flow by the correlation of individual particles to the reaction plane, it is also possible to measure flow by the correlation of two particles to each other. The advantage of this method is that one does not have to determine the reaction plane. If we write the azimuthal angle distribution of two particles A and B, which are correlated to a reaction plane as

$$\frac{dN^A}{d\phi^A} \propto 1 + \sum_n 2v_n^A \cos[n(\phi^A - \Psi_n)], \tag{1}$$

$$\frac{dN^B}{d\phi^B} \propto 1 + \sum_n 2v_n^B \cos[n(\phi^B - \Psi_n)], \tag{2}$$

then the azimuthal angle distributions for the two particle correlations can be written as

$$\frac{dN^{AB}}{d\phi^{AB}} \propto 1 + \sum_n 2v_n^A v_n^B \cos[n(\phi^A - \phi^B)] \tag{3}$$

$$\equiv 1 + \sum_n 2c_n \cos[n(\phi^A - \phi^B)]. \tag{4}$$

Instead of measuring v_n, this paper presents measurements of c_n, the coefficient of the Fourier fit to the correlation functions, because the factorization $c_n = v_n^A v_n^B$ holds only at low p_T, where the two particles are correlated with the same event plane [24]. This relation breaks down when considering high-p_T particles that are coming from the nonflow contributions such as jet fragmentation.

II. EXPERIMENT AND DATASET

A detailed description of the PHENIX detector system can be found elsewhere [25]. The principal detectors used in this analysis are the beam-beam counters (BBCs), the muon-piston calorimeter (MPC) and the electromagnetic calorimeter (EMCal). The BBCs are located north (BBCN, $3.1 < \eta < 3.9$, d-going) and south (BBCS, $-3.9 < \eta < -3.1$, Au-going) of the interaction point, covering the full azimuth and are sensitive to charged particles. In $d+\mathrm{Au}$ collisions, the Au ions are accelerated in the Au-going direction. The MPCs, which are high resolution electromagnetic calorimeters, are also located north (MPCN, $3.1 < \eta < 3.9$) and south (MPCS, $-3.7 < \eta < -3.1$) of the interaction point, in front of the BBCs, and cover the full azimuth. The south (north) MPC comprise 192 (220) $PbWO_4$ crystal towers with 20.2 X_0 or 0.89 λ_I [26]. The EMCal is located in the central (CNT) arms with pseudorapidity range $|\eta| < 0.35$ and covering two $\pi/2$ segments of the full azimuth. Figure 1 shows the acceptance of each relevant PHENIX detector subsystem in ϕ-η coordinates.

The $d+\mathrm{Au}$ and $p+p$ collision data used in this analysis were recorded in 2008 at RHIC. The events triggered by a high energy deposit in a 4×4 tower region of the EMCal in coincidence with the minimum bias (MB) requirement were selected in both the $p+p$ and $d+\mathrm{Au}$ data sets. The MB trigger was defined as the coincidence of at least one hit in the BBCS and BBCN. A z-vertex cut of $|z| < 30$ cm is applied, using the vertex calculated from the BBC timing information. The energy threshold of the 4×4 towers is set to be 2.8 GeV; however, due to the energy smearing effect, the towers also sample hits with lower energies but with lower efficiency. The number of recorded events was 2.85×10^8 (9.64×10^{10} MB

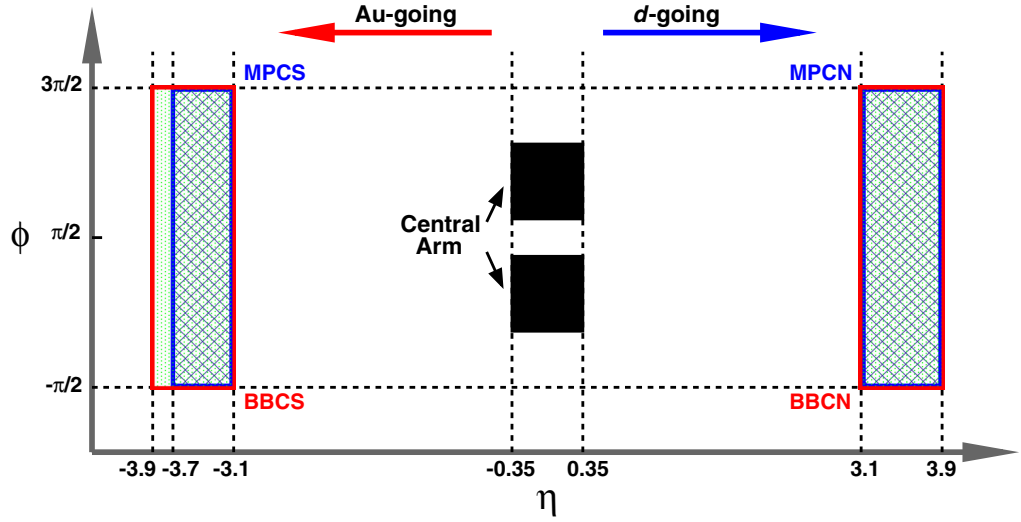

FIG. 1. Configuration in azimuth and pseudorapidity (ϕ-η) coordinates of the PHENIX detector subsystems used in this analysis. The BBC and MPC detectors each cover 2π in azimuth in the forward and backward directions, while the two PHENIX central arms each subtend $\pi/2$ in azimuth.

equivalent) for the $p+p$ and 6.51×10^8 (1.40×10^{11} MB equivalent) for the $d+$Au collisions, which made it possible to measure the π^0-triggered long-range correlations up to $p_T = 11$ GeV/c. In the case of $d+$Au collisions, centrality was defined by the total charge deposited in BBCS (Au-going direction). Seven partially overlapping centrality bins have been considered, from the most central (0%–5%) to the most peripheral (60%–88%) collisions [27].

III. ANALYSIS

The long-range two-particle correlation functions are constructed by pairing a high-p_T π^0 ("trigger" particle) found in the PHENIX EMCal with the energy deposit $E_{\rm dep}$ in each tower of one of the MPCs ("associated" hit). In the following sections we describe (i) the π^0 identification, (ii) construction of the initial azimuthal correlation functions, (iii) correction for combinatoric background in the π^0 sample, and (iv) fitting the corrected correlation functions with a harmonic expansion. Throughout this paper the results for central-MPC south (CNT-MPCS) and central-MPC north (CNT-MPCN) correlations are shown separately.

A. π^0 selection

Each trigger π^0 was measured in the EMCal via the $\pi^0\to\gamma\gamma$ decay channel using photon showers reconstructed using the standard PHENIX method [28–30]. The photon showers were identified using a shower-shape cut [31]. A cut on the energy asymmetry of the photon pair $\alpha = |E_1 - E_2|/(E_1 + E_2) < 0.7$ has been applied to reduce the combinatoric background. A sample $\gamma\gamma$ invariant mass plot is shown in Fig. 2 for pairs with pair $p_T > 3$ GeV/c. The π^0 mass region was defined as $0.12 < m_{\gamma\gamma} < 0.16$ GeV/c^2, and every measured pair in this range was used in compiling the initial correlation functions, binned according to pair p_T.

As shown in Fig. 2, the π^0 peak is quite prominent in the pair mass spectrum, on top of a small background continuum due primarily to combinatoric pairs. We estimated the level of this background in terms of the signal/background ratio S/B within the chosen π^0 mass window as shown in Fig. 3. The ratio was used for subtracting the combinatoric background contribution in the correlation functions, as explained in Sec. III C.

B. Initial correlation functions

The procedure used to construct the initial π^0-MPC correlation functions is essentially the same as was used in our earlier analysis of correlation of central-arm charged tracks

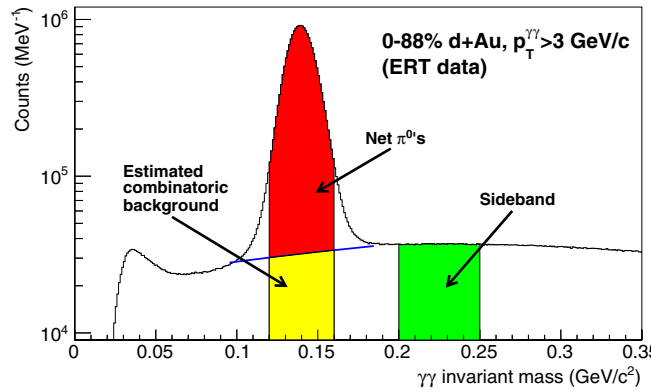

FIG. 2. Invariant mass distribution for $\gamma\gamma$ pairs from $d+$Au collisions as measured in the PHENIX central arm EMCal. The (red) shaded "Net π^0" peak is clearly visible above a small (yellow) shaded "Estimated combinatoric background" in the same mass window $0.12 < m_{\gamma\gamma} < 0.16$ GeV/c^2 (note the semilogarithmic scale). We estimate the combinatoric background by interpolating linearly between two points outside the peak, as shown by the (blue) line, which is obtained by fitting around the peak with a combined Gaussian and linear function. The purely combinatoric pairs in the shaded (green) "Sideband" region are used to correct the correlation functions for the effects of background pairs in the peak region (see Sec. III C).

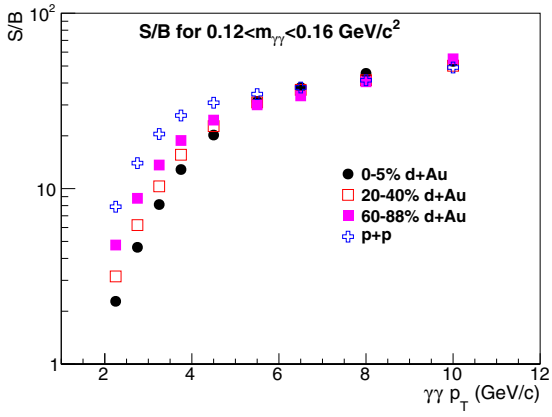

FIG. 3. Centrality and $\gamma\gamma$ p_T dependence of the signal to combinatoric background ratio (S/B) for pairs in the $0.12 < m_{\gamma\gamma} < 0.16$ GeV/c^2 mass window.

with MPC towers in $d+$Au and $p+p$ collisions [10]. Over a selected event sample and π^0 p_T bin, we compile the relative azimuthal angle distribution, $S(\Delta\phi, p_T)$, between $\gamma\gamma$ pairs in a given mass window and MPC towers in the same event:

$$S(\Delta\phi, p_T) = \frac{d\left(w_{\text{tower}} N^{\gamma\gamma(p_T)-\text{tower}}_{\text{Same event}}\right)}{d\Delta\phi}, \tag{5}$$

where $\Delta\phi = \phi_{\gamma\gamma} - \phi_{\text{tower}}$ is the azimuthal opening angle between the $\gamma\gamma$ pair-sum momentum direction and a line to the center of the MPC tower. We choose the weighting for each tower to be the transverse energy $w_{\text{tower}} = E_{\text{dep}} \sin(\theta_{\text{tower}})$, where E_{dep} is the energy deposit in that tower and θ_{tower} is the angular position of the tower with respect to the beam line. The w_{tower} introduces a p_T spectrum weight on the hit frequency in the MPC. The MPC towers with deposited energy $E_{\text{dep}} > 0.3$ GeV were selected to avoid the background from noncollision noise sources (≈75 MeV) and to cut out the deposits by minimum ionizing particles (≈245 MeV). To maximize statistics the energy is lowered compared to the one used in a previous publication [10].

In addition to physical pair correlations from the collisions, the shape of the same-event distribution $S(\Delta\phi, p_T)$ will reflect the effects of detector acceptance, detector inefficiencies, and kinematic cuts. We estimated these instrumental effects by constructing a mixed-event distribution $M(\Delta\phi, p_T)$ [Eq. (5)], but using $\gamma\gamma$ pairs from one event and MPC towers from a different event in the same event class (centrality and π^0 p_T). We then correct for instrumental effects by constructing the correlation function $C^X(\Delta\phi, p_T)$, for any particular choice X of $\gamma\gamma$ pair selection criterion

$$C^X(\Delta\phi, p_T) = \frac{S^X(\Delta\phi, p_T)}{M^X(\Delta\phi, p_T)} \frac{\int M^X(\Delta\phi, p_T) d\Delta\phi}{\int S^X(\Delta\phi, p_T) d\Delta\phi} \tag{6}$$

Both the same-event numerator and the mixed-event denominator have been normalized by their respective integrals.

C. Combinatoric sideband correction

The initial correlation function is constructed using all pairs in the π^0 mass window, which necessarily includes an admixture of both true π^0 pairs and background pairs. Therefore, it will not reflect simply the true π^0-MPC correlation but rather a weighted average of the correlations of true π^0 pairs and those of background pairs. Though the background is typically a small fraction of the signal, as shown in Fig. 3, we carried out the following correction to remove any influence from the background pairs.

We denote the initial correlation function constructed using all photon pairs in the π^0 mass peak region as $C^{S+B}(\Delta\phi, p_T)$, because it contains correlations from both signal and background pairs. We then approximate the correlation function $C^B(\Delta\phi, p_T)$ that would result from using the background pairs only, by constructing a correlation function according to Eq. (6), but with pairs chosen from the "sideband" mass region $0.20 < m_{\gamma\gamma} < 0.25$ GeV/c^2 (see Fig. 2). We then derive the true π^0-MPC correlation function $C(\Delta\phi, p_T)$, which would result from including only the true π^0 decay pairs, by inverting the weighted average via

$$C(\Delta\phi, p_T) = \left(1 + \frac{B}{S}\right) C^{S+B}(\Delta\phi, p_T) - \frac{B}{S} C^B(\Delta\phi, p_T), \tag{7}$$

where B/S is the background-to-signal ratio in the peak region, which is the reciprocal of the number shown in Fig. 3. In practice, this correction for background pairs is very small; it does not change the harmonic amplitudes of the correlation function (see Sec. III D) by more than a few percent of their value in the lowest S/B cases and becomes negligible as S/B increases toward higher p_T.

D. Harmonic expansion fitting

Our objective in this analysis is to examine the shapes of the π^0-MPC correlation functions across π^0 p_T and collision system centrality classes. We quantify each correlation function by fitting them to an expansion in Fourier terms over $\Delta\phi$ up to fourth order via

$$C(\Delta\phi, p_T) = B_0 \left(1 + \sum_{n=1}^{4} 2\, c_n(p_T) \cos(n\Delta\phi)\right). \tag{8}$$

The fits were optimized using only the statistical errors in the final correlation functions. The fit for each p_T and event class combination has five parameters: the four c_n and an overall normalization. Each correlation function was compiled in 20 bins of $\Delta\phi$, leaving 15 degrees of freedom (NDF) for each fit. The $C(\Delta\phi, p_T)$ with fit functions are shown in Sec. IV and in the Appendix. The χ^2/NDF goodness-of-fit values are compiled and shown in Fig. 4. There is no particular structure seen with π^0 p_T or event class, and the distribution agrees with what would be expected for a χ^2 estimator.

When we fit the correlation functions with c_2 fixed to zero, the χ^2/NDF's are found to be as high as ≈40 around $p_T = 3$ GeV/c, and do not reach $\chi^2/\text{NDF} \approx 4$ before $p_T \approx 6$ GeV/c, for both 0%–5% central $d+$Au and $p+p$ collisions. This shows that the correlation functions have a significant second-order component.

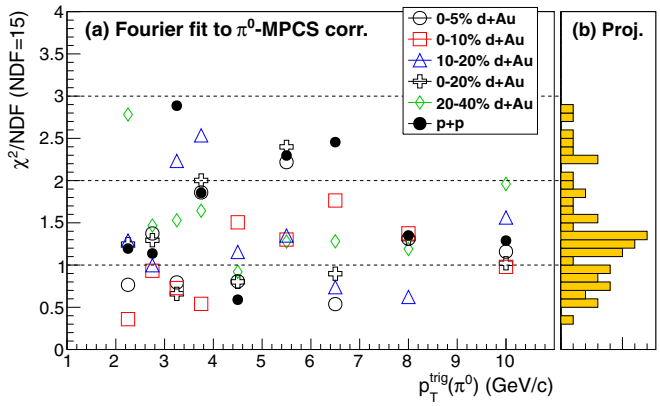

FIG. 4. (a) Goodness-of-fit parameter χ^2/NDF for the harmonic fits in Eq. (8) to the corrected π^0-MPCS correlation functions, for different centrality and π^0 p_T selections, and (b) their projection to the y axis.

E. Estimation of systematic errors

The systematic uncertainties of the measurement have been estimated as follows. The width of the π^0 extraction window as well as the location and width of the sideband have been varied in five different combinations as listed in Table I. Note that the case 0 corresponds to the standard windows in this analysis.

In the sixth case the original windows were kept as case 0 but the asymmetry cut was changed to $\alpha < 0.5$. Following the exact same procedure for obtaining the true π^0-MPC correlation functions as described in the previous sections, the correlation functions for the six cases were obtained and the values of c_2 and $-c_2/c_1$ were re-calculated. The deviations for the case-0 values, with respect to the standard result, were calculated and averaged over the six cases. The averaged deviations are the systematic uncertainties. The resulting uncertainties on c_2 are 2% for $p+p$ (all p_T), and for the 0%–5% $d+$Au (worst case) they are 8% at 2 GeV/c and 3% at 6 GeV/c for CNT-MPCS (Au-going). The uncertainty for the $-c_2/c_1$ is very similar to that of c_2 owing to a smaller uncertainty of c_1. This study was also performed for CNT-MPCN (d-going) correlations, obtaining 4% (2 GeV/c) and 2% (6 GeV/c) for $p+p$ and 12% (2 GeV/c) and 3% (6 GeV/c) for the 0%–5% $d+$Au. Both CNT-MPCS and CNT-MPCN show consistent systematic uncertainties given the large statistical uncertainties in the CNT-MPCN correlations. Considering the better statistical precision for the CNT-MPCS correlations, we quoted the errors for them as the systematic uncertainties for the final results. There is a possible systematic uncertainty associated with the mixed event distributions $M(\Delta\phi, p_T)$. This uncertainties are effectively folded during the procedure of the systematic uncertainty estimate described above.

TABLE I. Combination of π^0 extraction and sideband windows for estimating systematic errors. Note that case 0 corresponds to the standard windows in this analysis.

Case	π^0 window (GeV/c^2)	Sideband window (GeV/c^2)
0	0.12–0.16	0.20–0.25
1	0.12–0.16	0.25–0.30
2	0.12–0.16	0.06–0.09
3	0.12–0.16	0.06–0.09 + 0.20–0.30
4	0.10–0.18	0.20–0.25
5	0.13–0.15	0.20–0.25

IV. RESULTS AND DISCUSSIONS

We present the corrected correlation functions [Eq. (7)], together with the four-term Fourier fit functions [Eq. (8)], across a range of collision systems and π^0 p_T bins, for both CNT-MPCS (Au-going) and CNT-MPCN (d-going) combinations. Representative samples for the bins $3 < p_T < 3.5$ GeV/c and $5 < p_T < 6$ GeV/c appear in Figs. 5 and 6, while the full sets are shown in the Appendix.

The correlation functions are largely dominated by a dipole component ($n = 1$), and higher components ($n > 1$) contribute to form a near-side enhancement structure in the near side ($\Delta\phi \approx 0$) of the functions. The dipole component is usually attributed to the back-to-back dijet contribution and momentum conservation in the system. With the large psuedorapidity gap employed ($|\Delta\eta| > 3$), the near-side particles of the dijet triggered by π^0 ($|\eta| < 0.35$) will not form a peak at $\Delta\phi \approx 0$ in the MPCs ($3.1 < |\eta| < 3.9$). Therefore, the near-side enhancement is formed by other sources, possibly a quadrupole flow from a bulk medium. The characteristic structure is clearly visible for CNT-MPCS (Au-going), but not for CNT-MPCN (d-going). In addition, the structure is more prominent in the more central collisions (e.g., see the first plot in the Appendix),

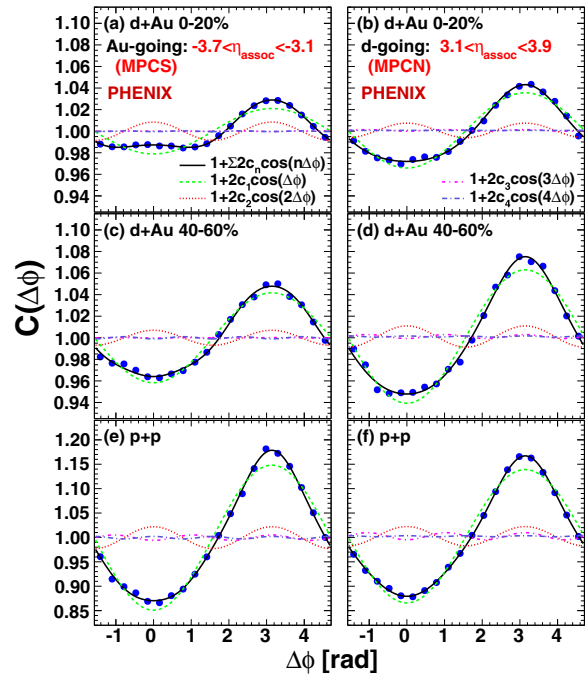

FIG. 5. Centrality dependence of correlation functions for $d+$Au and $p+p$ collisions at $\sqrt{s_{NN}}$ =200 GeV for π^0 in $|\eta_{\rm trig}| < 0.35$ (CNT). (a), (c), (e) π^0 are associated with the towers in MPCS (Au-going direction) and (b), (d), (f) MPCN (d-going direction), for $3 < p_T < 3.5$ GeV/c.

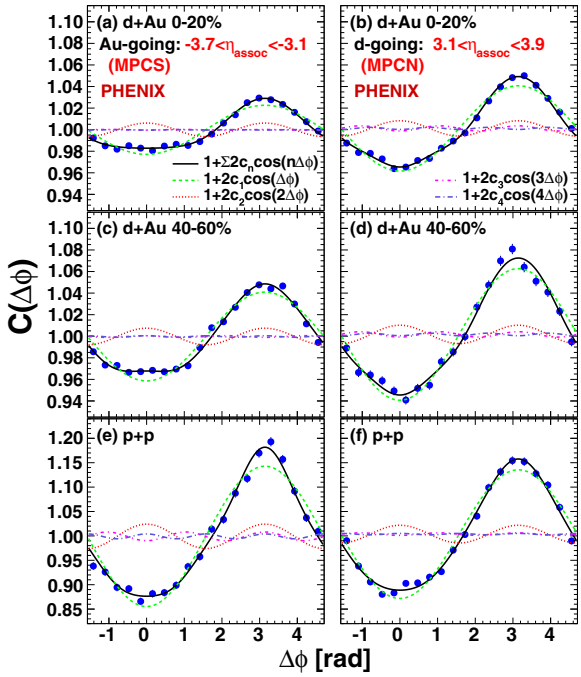

FIG. 6. The same as Fig. 5, except for $5 < p_T < 6$ GeV/c.

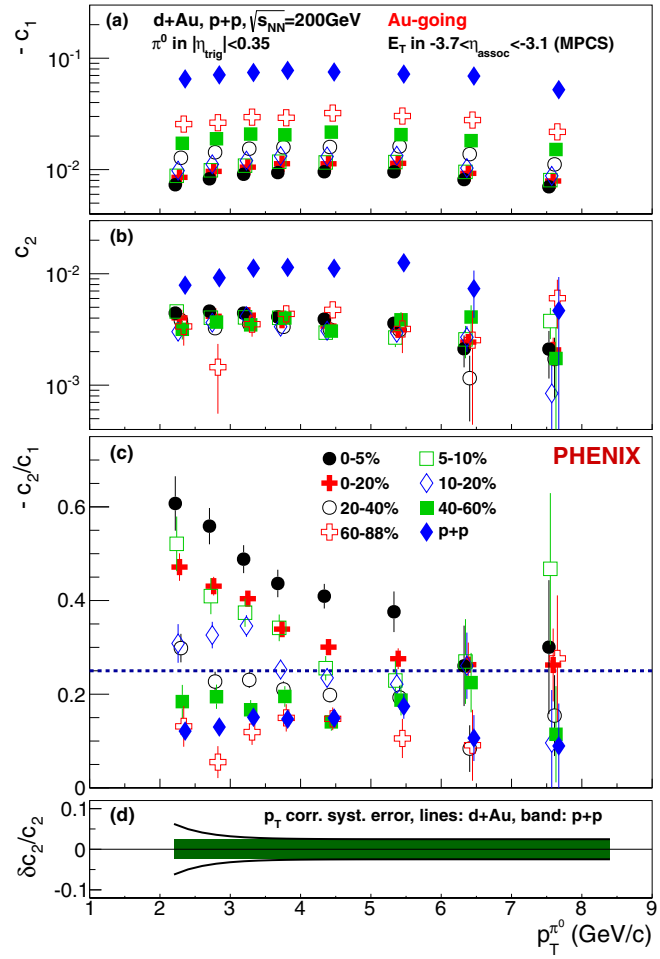

FIG. 7. Fourier fit coefficients for CNT-MPCS (Au-going) correlations, as a function of collision system and π^0 p_T: (a) the negative of the dipole coefficient, $-c_1$; (b) the quadrupole coefficient c_2; (c) the ratio $-c_2/c_1$; (d) fractional systematic uncertainty on the quadrupole coefficient c_2 for d + Au (lines) and $p + p$ (band). The dotted (blue) line at 0.25 in panel (c) marks the nominal threshold, above which the correlation function would exhibit a near-side local maximum (see text).

and it gradually disappears with both decreasing centrality and increasing p_T. The trend in the CNT-MPCS correlation hints that the structure has a characteristic similar to the hydrodynamical particle flow in $A + A$ collisions. Looking at the evolution of the individual Fourier-components c_i with centrality and p_T provides a richer and more quantitativxe picture. As seen in Figs. 5 and 6, the c_3 and c_4 are both very small, and are found to be consistent with zero within uncertainties. Therefore, we discuss here only the centrality and p_T dependence of the dipole (c_1) and quadrupole (c_2) coefficients.

The c_1 (dipole) values for CNT-MPCS correlations are summarized in Fig. 7(a). They exhibit a definite ordering with system size: the largest negative values are observed in $p + p$, the smallest ones in the most central d + Au. Similar ordering, albeit with smaller absolute differences, can be seen for CNT-MPCN in Fig. 8. This trend is similar to the decrease of the absolute value of c_1 with increasing multiplicity that was observed in Ref. [11]. If the negative c_1 at large $\Delta\eta$ is indeed a consequence of a dijet fragmentation into the CNT and MPC regions, then we would expect the effect to be diluted as the underlying event multiplicity increases. Because the overall multiplicity on the d-going side is smaller, we would also expect a larger magnitude for c_1 there compared with the Au-going direction, as seen in the data. Interestingly, the c_1 coefficients vary with p_T and have a maximum magnitude around 4–5 GeV/c. It may be related to the fact that this is the p_T region where hard scattering becomes dominant over bulk phenomena that govern particle production at lower p_T.

The p_T and centrality dependence of c_2 (quadrupole) values in CNT-MPCS and CNT-MPCN correlations are shown in panel (b) of Figs. 7 and 8, along with their p_T-correlated systematic uncertainties in panel (d). For $p + p$ collisions the two distributions are compatible, as expected for the symmetric system. The c_2 in $p + p$ collisions are roughly double those seen in d + Au (including the most peripheral bin), and the p_T dependence of their magnitudes is similar to that of the c_1. For d + Au the c_2 for CNT-MPCN and CNT-MPCS correlations are similar in magnitude, but with the CNT-MPCN showing a greater spread with centrality. The c_2 are small and decreasing as a function of p_T, but nonvanishing in the available p_T range, proving that the quadrupole component is present.

To gauge the magnitude of characteristic-structure correlations as a measure of a bulk property of the system, we calculated $-c_2/c_1$, the ratio of c_2 (quadrupole) to $-c_1$ (dipole), for all $p + p$ and d + Au systems, as shown in Fig. 7(c). For the CNT-MPCS correlations [Fig. 7(a)] the data exhibit a well-defined ordering with system centrality, within errors, from the most central d + Au down to the most peripheral (60%–88%) which is consistent with the $p + p$. We then see a smooth evolution from the most central collisions observed at

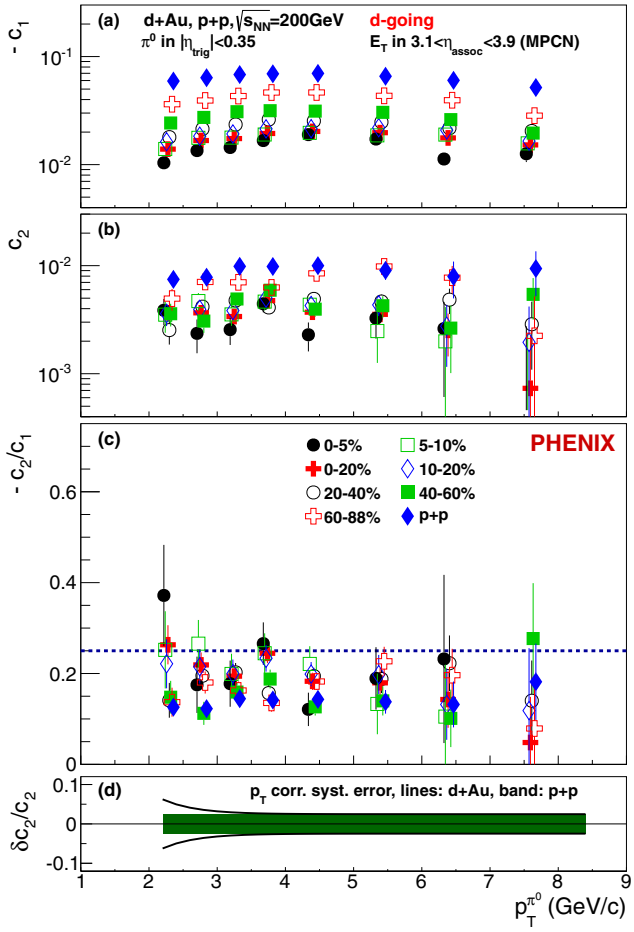

FIG. 8. The same as Fig. 7, except for CNT-MPCN (d-going) correlations.

lowest p_T, where the near-side correlations are most prominent and which would be expected to have the largest contribution from a collective source, to the more peripheral and higher p_T limit, where the near-side correlation vanishes and elementary processes are expected to dominate. The trend is very different for CNT-MPCN correlations [Fig. 8(b)]. Here all the $-c_2/c_1$ ratios are consistent for both $d+\text{Au}$ and $p+p$ collisions, indicating no additional near-side correlations in $d+\text{Au}$ over $p+p$ collisions for any system across the entire π^0 p_T range studied here. There is also no visible ordering of $-c_2/c_1$ with system centrality for $p_T > 2.5$ GeV/c, in contrast to the CNT-MPCS case, within uncertainties.

The c_1 and c_2 for the symmetric $p+p$ collisions are somewhat different between CNT-MPCS and CNT-MPCN, which results from the difference of psuedorapidity coverage in MPCN ($3.1 < \eta < 3.9$) versus MPCS ($-3.7 < \eta < -3.1$). The fact that the $-c_1/c_2$ are very consistent indicates that the same phenomenon is observed in each direction.

Recently, attempts have been made to develop methods that effectively subtract the nonflow contributions present in two-particle correlations, as measured in $p/d+A$ collisions [4,8,32,33]. Despite their differences, all of these methods rely on the assumption that one can identify a class of events (usually $p+p$ or peripheral $p/d+A$) with low enough multiplicity such that the corresponding correlation function can be attributed entirely to nonflow. However, there is currently no consensus in the field regarding how the subtraction procedure should be carried out. This paper therefore focuses on the shape analysis of the correlation functions, leaving nonflow subtraction outside of the scope. However, we point out that the quantity $-c_2/c_1$ encodes some information about the relative strength of nonflow, and its comparison between collision systems can provide useful insight.

Another shape study of the near-side correlations can be performed by examining the second derivative of $dN/d(\Delta\phi)$. If we approximate the $n > 2$ coefficients as negligible ($c_3 \approx c_4 \approx 0$), then the condition of having a local maximum at $\Delta\phi = 0$ corresponds to

$$(\partial^2/\partial\Delta\phi^2)(dN/d\Delta\phi) \propto -c_1 - 4c_2 < 0. \tag{9}$$

The observed positive c_2 and negative c_1 lead us to use the threshold of $-c_2/c_1 > 0.25$ as the condition indicating that a near-side correlation with a local maximum is present in the correlation function, as also pointed out in the literature [34]. The dotted lines in panel (c) in Figs. 7 and 8 indicate this threshold. For the CNT-MPCS correlations the data are clearly above the threshold for the more central $d+\text{Au}$ collisions, out to 20%, and for $p_T < 6$ GeV/c, indicating that the shapes have a local maximum. For the CNT-MPCN correlations, all the $-c_2/c_1$ ratios consistently lie below 0.25 for both $d+\text{Au}$ and $p+p$ collisions, indicating no local maximum. It should be noted that the absence of a local maximum does not necessarily imply that the near-side contribution is absent.

We now examine the system and centrality dependence of the correlation functions. Figure 9 shows c_1, c_2, and $-c_2/c_1$ as a function of the mean number of collision participants N_{part} [27] for the two selected p_T ranges 3–3.5 GeV/c and 5–6 GeV/c.

The values for both CNT-MPCS and CNT-MPCN are shown. The smooth decrease of c_1 with N_{part} is clearly seen for both p_T selections, but the decrease of c_1 for the CNT-MPCS is more rapid compared to that of CNT-MPCN. In contrast, c_2 is flat or exhibits little increase (decrease) as a function of N_{part} for CNT-MPCN (CNT-MPCS) correlations, except for the lowest N_{part}. In $-c_2/c_1$, where individual $-c_1$ and c_2 trends are combined, the data for CNT-MPCS show a smooth rising trend, stronger for the lower p_T selection, while $-c_2/c_1$ for CNT-MPCN correlations displays no evolution with N_{part} at all from $p+p$ to the most central $d+\text{Au}$ collisions. This observation clearly shows again that the characteristic structure is clearly seen in the Au-going direction, rather than in the d-going direction, and ceases at high p_T, which is a characteristic similar to the hydrodynamical particle flow in $A+A$ collisions.

The centrality dependence of $-c_1/c_2$ can be understood in terms of the asymmetry of the charged particle pseudorapidity distributions with respect to $\eta = 0$ in $d+\text{Au}$ collisions [35]. When going to greater centrality, the results indicate that the characteristic structure is shifted in the Au-going direction, similar to the charged-particle pseudorapidity distributions. This is consistent with the findings of the STAR experiment [11] in the region where the p_T ranges overlap. There is a possible fluctuation of the event plane as a function of psuedorapidity as observed by the CMS experiment at the LHC

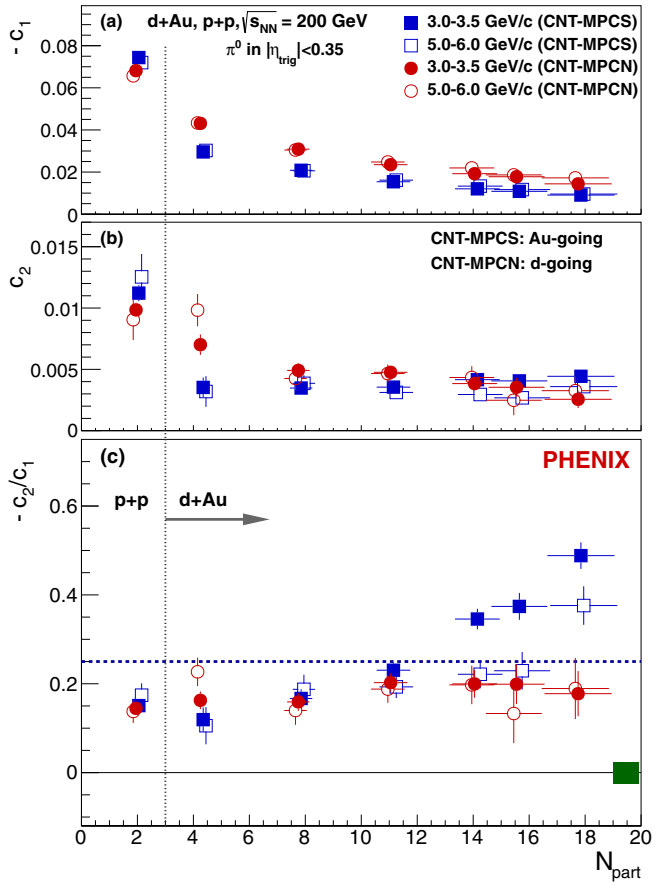

FIG. 9. System centrality dependence of correlation coefficients (a) $-c_1$, (b) c_2, and (c) the ratio $-c_2/c_1$ as a function of N_{part}. Results for both CNT-MPCS (Au-going direction) and CNT-MPCN (d-going direction) correlations are each shown for two p_T regions. The box (green) shows the systematic uncertainty on the $-c_2/c_1$ ratio, which is constant with N_{part}. The uncertainties on the N_{part} estimates are shown on each data point as horizontal error bars.

[36]. Although this may partly explain the centrality-dependent difference between CNT-MPCN and CNT-MPCS, our measurements lack the precision to gauge the effect. These results provide a strong argument for studying long-range correlations in asymmetric systems separately in the forward/backward directions.

V. SUMMARY

We have measured long-range azimuthal correlations between high-transverse-momentum ($2 < p_T < 11$ GeV/c) π^0 observed at midrapidity ($|\eta| < 0.35$) and particles produced either at forward ($3.1 < \eta < 3.9$) or backward ($-3.7 < \eta < -3.1$) rapidity in $d+\text{Au}$ and $p+p$ collisions at $\sqrt{s_{NN}} =$ 200 GeV. The centrality- and p_T-dependent two-particle correlations were fitted with a Fourier series up to the fourth term. While the third and fourth coefficients (c_3,c_4) were consistent with zero within uncertainties, the c_1 (dipole) values exhibit a definite ordering with the system size both in the Au-going and d-going directions. The c_2 (quadrupole) values exhibit similar magnitudes for both directions. However, $-c_2/c_1$ values exhibit well-defined ordering with system centrality and decrease with increasing p_T in the Au-going direction, while the values are consistent over all systems and p_T in the d-going direction. This implies that the characteristic structure clearly exists in the Au-going direction, rather than in the d-going direction, and ceases at high p_T, which is a characteristic similar to the hydrodynamical particle flow in $A+A$ collisions. The difference of the behavior in the Au-going and the d-going directions can be understood from the fact that the characteristic structure is shifted in the Au-going direction toward more central collisions, similar to the charged-particle pseudorapidity distributions. This suggests that looking at two directions in asymmetric systems is essential.

ACKNOWLEDGMENTS

We thank the staff of the Collider-Accelerator and Physics Departments at Brookhaven National Laboratory and the staff of the other PHENIX participating institutions for their vital contributions. We acknowledge support from the Office of Nuclear Physics in the Office of Science of the Department of Energy, the National Science Foundation, Abilene Christian University Research Council, the Research Foundation of SUNY, and Dean of the College of Arts and Sciences, Vanderbilt University (USA); the Ministry of Education, Culture, Sports, Science, and Technology and the Japan Society for the Promotion of Science (Japan); Conselho Nacional de Desenvolvimento Científico e Tecnológico and Fundação de Amparo à Pesquisa do Estado de São Paulo (Brazil); the Natural Science Foundation of China (People's Republic of China); the Croatian Science Foundation and Ministry of Science and Education (Croatia); the Ministry of Education, Youth and Sports (Czech Republic), Centre National de la Recherche Scientifique, Commissariat à l'Énergie Atomique, and Institut National de Physique Nucléaire et de Physique des Particules (France); Bundesministerium für Bildung und Forschung, Deutscher Akademischer Austausch Dienst, and Alexander von Humboldt Stiftung (Germany); a J. Bolyai Research Scholarship, EFOP, the New National Excellence Program (ÚNKP), NKFIH, and OTKA (Hungary); the Department of Atomic Energy and Department of Science and Technology (India); the Israel Science Foundation (Israel); the Basic Science Research Program through NRF of the Ministry of Education (Korea); Physics Department, Lahore University of Management Sciences (Pakistan); the Ministry of Education and Science, Russian Academy of Sciences, Federal Agency of Atomic Energy (Russia); VR and Wallenberg Foundation (Sweden); the U.S. Civilian Research and Development Foundation for the Independent States of the Former Soviet Union, the Hungarian American Enterprise Scholarship Fund, the US-Hungarian Fulbright Foundation, and the US-Israel Binational Science Foundation.

APPENDIX

Figures 10–13 show data points of the normalized correlation functions in CNT-MPCS and CNT-MPCN for all $d+\text{Au}$ centralities and in p_T bins of the trigger π^0 in CNT

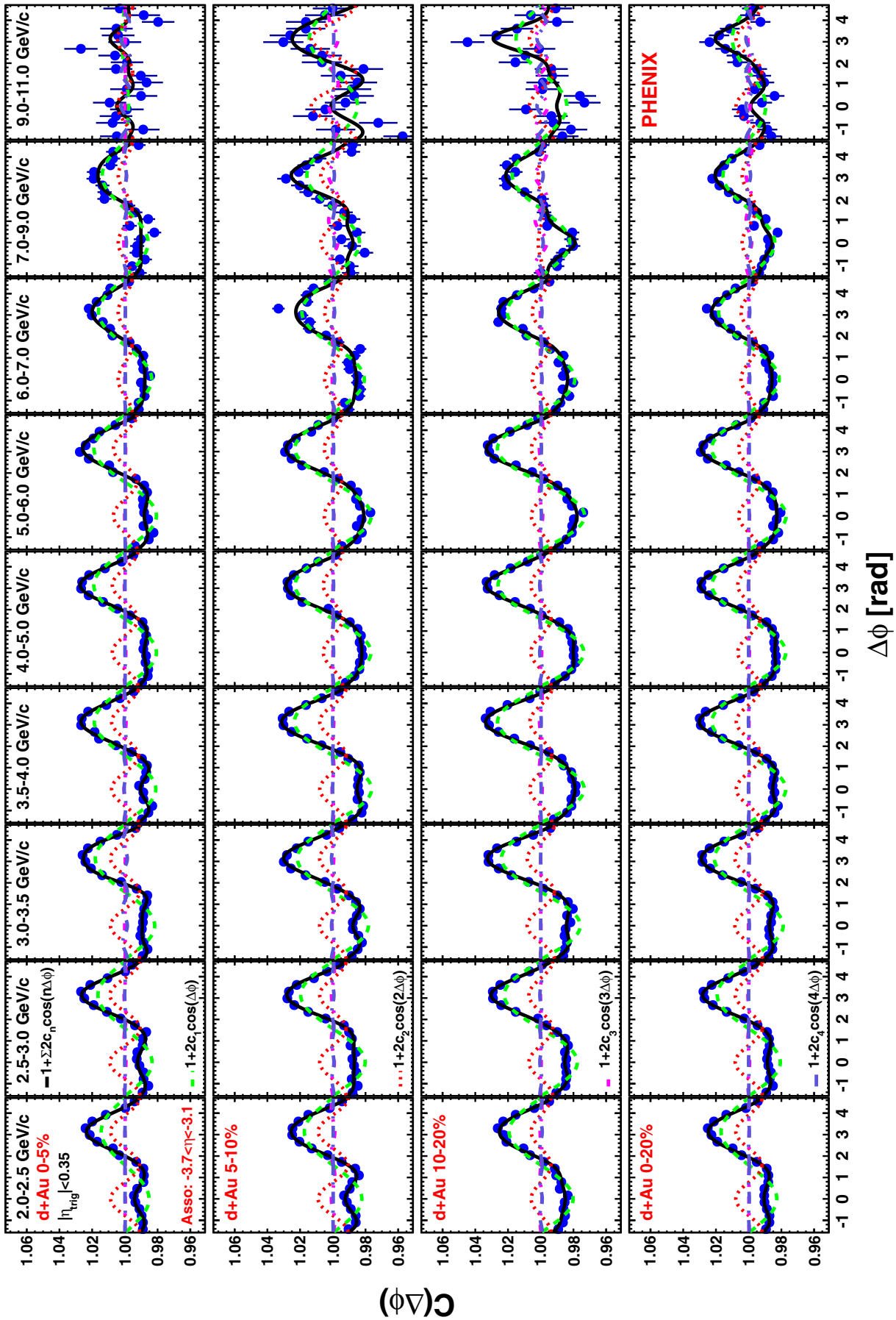

FIG. 10. CNT-MPCS correlation functions for 0%–5%, 5%–10%, 10%–20%, 0%–20% d + Au collisions for $2.0 < p_T < 11$ GeV/c.

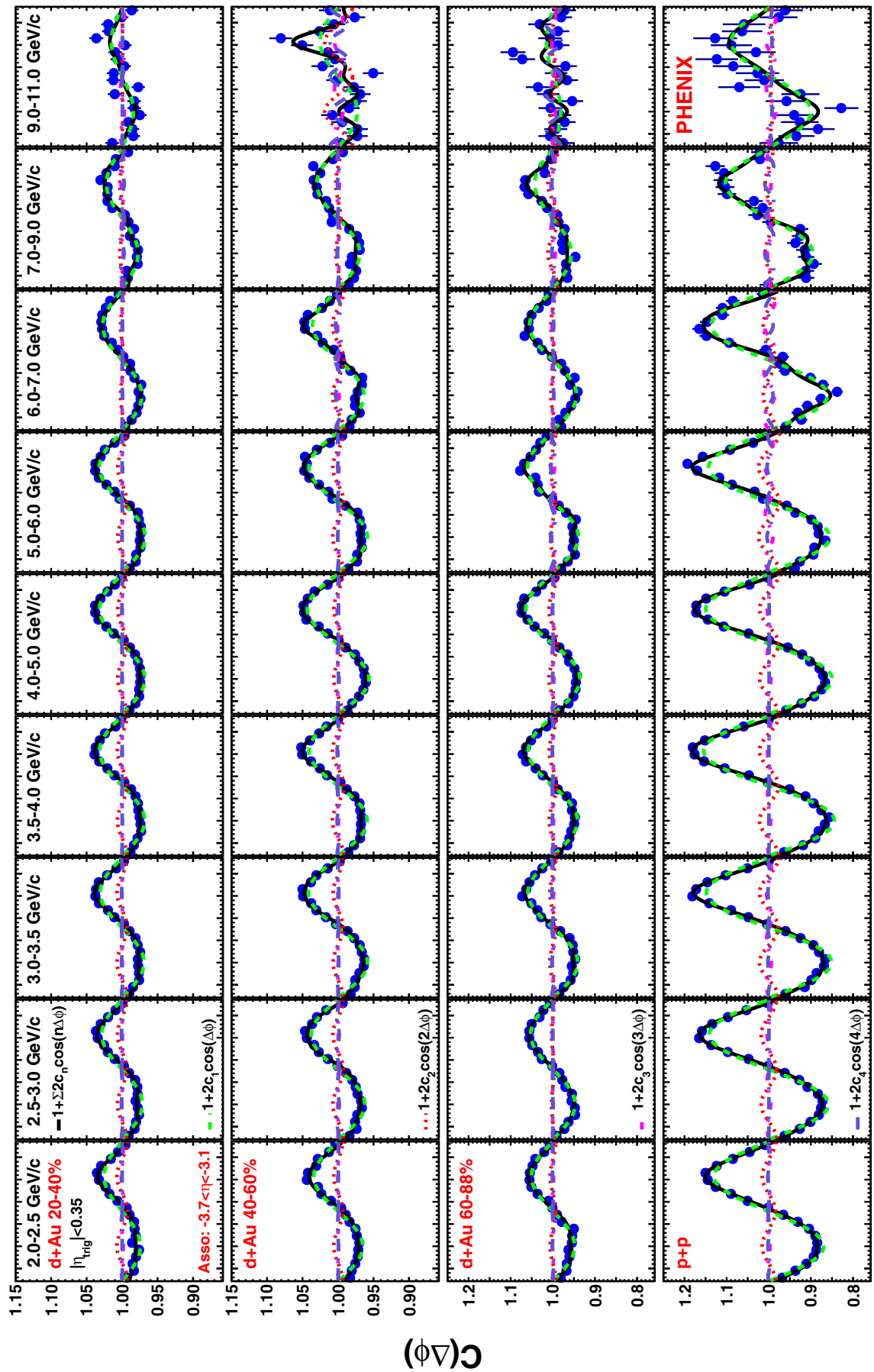

FIG. 11. CNT-MPCS correlation functions for 20%–40%, 40%–60%, 60%–88% d + Au collisions and $p + p$ collisions for $2.0 < p_T < 11$ GeV/c.

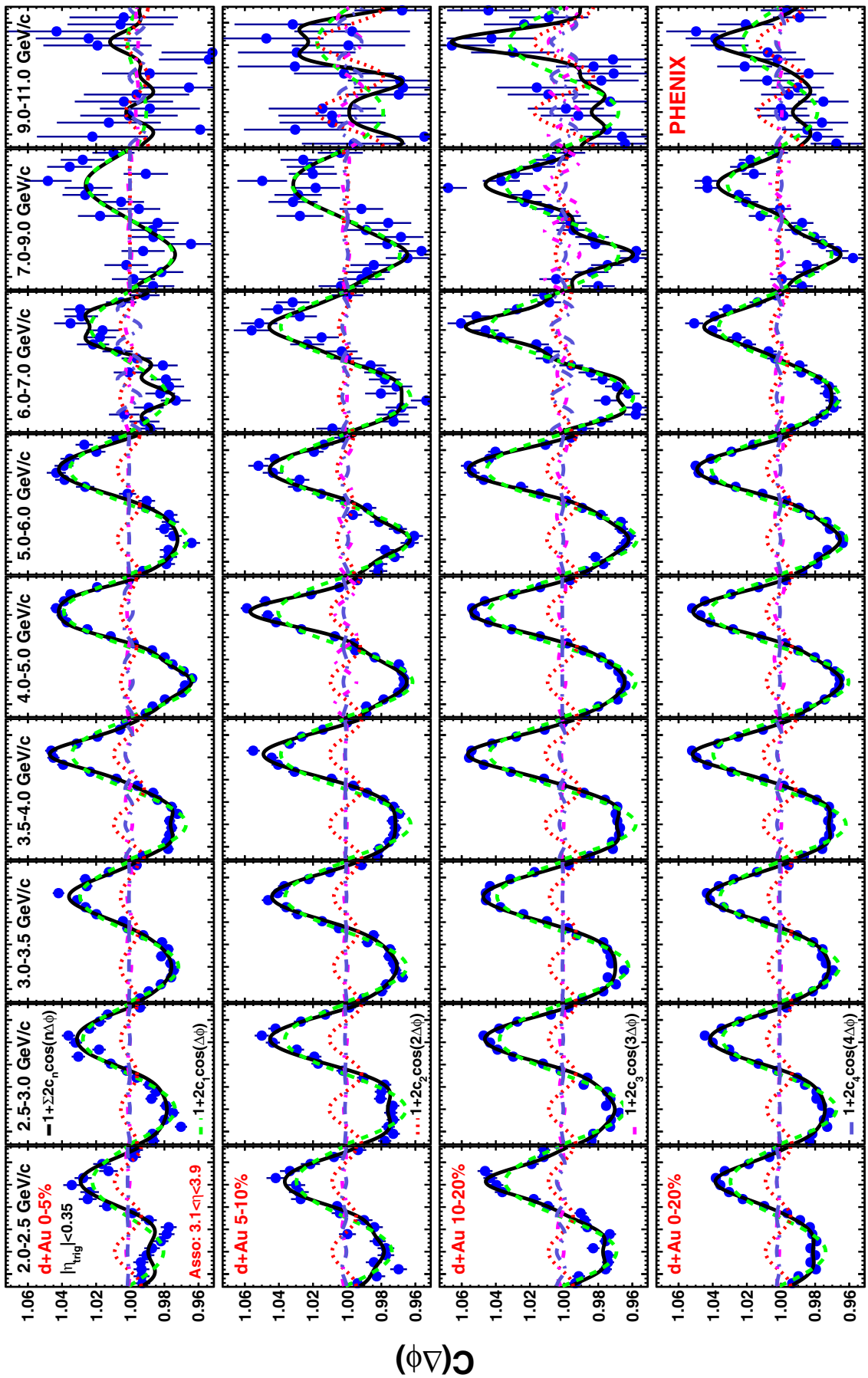

FIG. 12. CNT-MPCN correlation functions for 0%–5%, 5%–10%, 10%–20%, 0%–20% d + Au collisions for $2.0 < p_T < 11$ GeV/c.

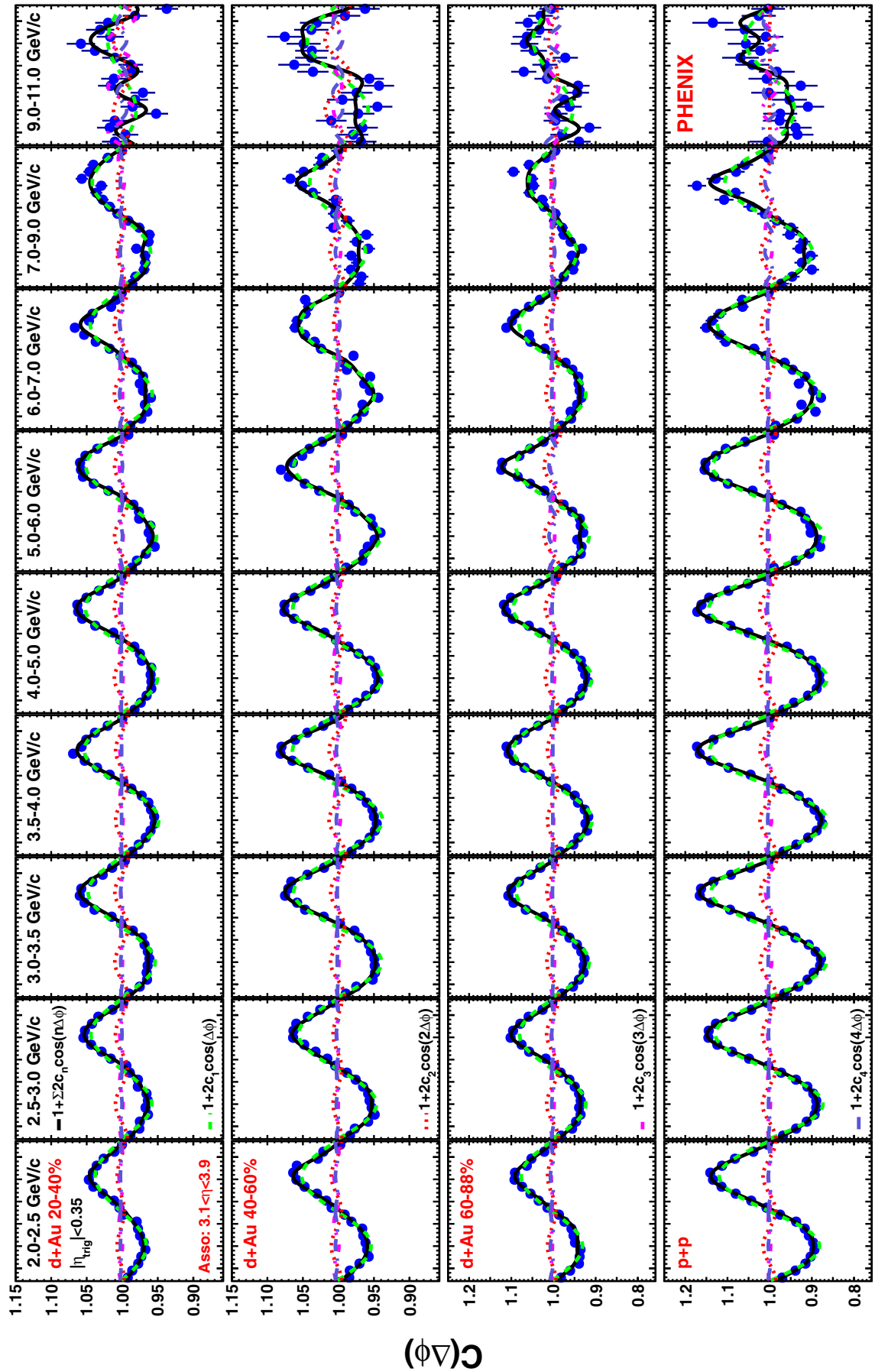

FIG. 13. CNT-MPCN correlation functions for 20%–40%, 40%–60%, 60%–88% d + Au collisions and $p + p$ collisions for $2.0 < p_T < 11$ GeV/c.

($|\eta_{\rm trig}| < 0.35$), along with the fitted Fourier-components and their sum. Note the changes in y scale from Figs. 10 and 12 to Figs. 11 and 13. Although the correlation functions are shown up to $p_T = 11$ GeV/c, it is clear that the statistical precision is poor for the 9–11 GeV/c data. Therefore, the c_1, c_2, and $-c_2/c_1$ in this paper are shown only up to 9 GeV/c.

[1] U. Heinz and R. Snellings, Collective flow and viscosity in relativistic heavy-ion collisions, Annu. Rev. Nucl. Part. Sci. **63**, 123 (2013).

[2] J.-Y. Ollitrault, Relativistic hydrodynamics for heavy-ion collisions, Eur. J. Phys. **29**, 275 (2008).

[3] V. Khachatryan *et al.* (CMS Collaboration), Observation of long-range near-side angular correlations in proton-proton collisions at the LHC, J. High Energy Phys. 09 (2010) 091.

[4] S. Chatrchyan *et al.* (CMS Collaboration), Observation of long-range near-side angular correlations in proton-lead collisions at the LHC, Phys. Lett. B **718**, 795 (2013).

[5] B. Abelev *et al.* (ALICE Collaboration), Long-range angular correlations on the near and away side in p-Pb collisions at $\sqrt{s_{NN}} = 5.02$ TeV, Phys. Lett. B **719**, 29 (2013).

[6] G. Aad *et al.* (ATLAS Collaboration), Observation of Associated Near-Side and Away-Side Long-Range Correlations in $\sqrt{s_{NN}} =$ 5.02 TeV Proton-Lead Collisions with the ATLAS Detector, Phys. Rev. Lett. **110**, 182302 (2013).

[7] G. Aad *et al.* (ATLAS Collaboration), Measurement of long-range pseudorapidity correlations and azimuthal harmonics in $\sqrt{s_{NN}} = 5.02$ TeV proton-lead collisions with the ATLAS detector, Phys. Rev. C **90**, 044906 (2014).

[8] M. Aaboud *et al.* (ATLAS Collaboration), Measurements of long-range azimuthal anisotropies and associated Fourier coefficients for pp collisions at $\sqrt{s} = 5.02$ and 13 TeV and p+Pb collisions at $\sqrt{s_{NN}} = 5.02$ TeV with the ATLAS detector, Phys. Rev. C **96**, 024908 (2017).

[9] A. Adare *et al.* (PHENIX Collaboration), Quadrupole Anisotropy in Dihadron Azimuthal Correlations in Central d + Au Collisions at $\sqrt{s_{NN}} = 200$ GeV, Phys. Rev. Lett. **111**, 212301 (2013).

[10] A. Adare *et al.* (PHENIX Collaboration), Measurement of Long-Range Angular Correlation and Quadrupole Anisotropy of Pions and (Anti)Protons in Central d + Au Collisions at $\sqrt{s_{NN}} = 200$ GeV, Phys. Rev. Lett. **114**, 192301 (2015).

[11] L. Adamczyk *et al.* (STAR Collaboration), Long-range pseudorapidity dihadron correlations in d+Au collisions at $\sqrt{s_{NN}} =$ 200 GeV, Phys. Lett. B **747**, 265 (2015).

[12] A. Adare *et al.* (PHENIX Collaboration), Centrality-Dependent Modification of Jet-Production Rates in Deuteron-Gold Collisions at $\sqrt{s_{NN}} = 200$ GeV, Phys. Rev. Lett. **116**, 122301 (2016).

[13] C. Aidala *et al.*, Measurement of long-range angular correlations and azimuthal anisotropies in high-multiplicity p + Au collisions at $\sqrt{s_{NN}} = 200$ GeV, Phys. Rev. C **95**, 034910 (2017).

[14] C. Aidala *et al.* (PHENIX Collaboration), Measurements of Multiparticle Correlations in d + Au Collisions at 200, 62.4, 39, and 19.6 GeV and p + Au Collisions at 200 GeV and Implications for Collective Behavior, Phys. Rev. Lett. **120**, 062302 (2018).

[15] C. Aidala *et al.* (PHENIX Collaboration), Measurements of azimuthal anisotropy and charged-particle multiplicity in d + Au collisions at $\sqrt{s_{NN}} = 200$, 62.4, 39, and 19.6 GeV, Phys. Rev. C **96**, 064905 (2017).

[16] P. Bożek and W. Broniowski, Collective dynamics in high-energy proton-nucleus collisions, Phys. Rev. C **88**, 014903 (2013).

[17] A. Bzdak, B. Schenke, P. Tribedy, and R. Venugopalan, Initial state geometry and the role of hydrodynamics in proton-proton, proton-nucleus and deuteron-nucleus collisions, Phys. Rev. C **87**, 064906 (2013).

[18] P. Romatschke, Light-heavy ion collisions: A window into pre-equilibrium QCD dynamics? Eur. Phys. J. C **75**, 305 (2015).

[19] R. D. Weller and P. Romatschke, One fluid to rule them all: Viscous hydrodynamic description of event-by-event central p + p, p + Pb and Pb + Pb collisions at $\sqrt{s} = 5.02$ TeV, Phys. Lett. B **774**, 351 (2017).

[20] K. Dusling and R. Venugopalan, Comparison of the color glass condensate to dihadron correlations in proton-proton and proton-nucleus collisions, Phys. Rev. D **87**, 094034 (2013).

[21] Z.-W. Lin, C. M. Ko, B.-A. Li, B. Zhang, and S. Pal, Multiphase transport model for relativistic heavy ion collisions, Phys. Rev. C **72**, 064901 (2005).

[22] L. He, T. Edmonds, Z-W. Lin, F. Liu, D. Molnar, and F. Wang, Anisotropic parton escape is the dominant source of azimuthal anisotropy in transport models, Phys. Lett. B **753**, 506 (2016).

[23] S. Chatrchyan *et al.* (CMS Collaboration), Azimuthal Anisotropy of Charged Particles at High Transverse Momenta in Pb-Pb Collisions at $\sqrt{s_{NN}} = 2.76$ TeV, Phys. Rev. Lett. **109**, 022301 (2012).

[24] M. J. Tannenbaum, Highlights from BNL-RHIC, arXiv:1201.5900.

[25] K. Adcox *et al.* (PHENIX Collaboration), PHENIX detector overview, Nucl. Instrum. Methods Phys. Res., Sect. A **499**, 469 (2003).

[26] A. Adare *et al.* (PHENIX Collaboration), Measurement of transverse-single-spin asymmetries for midrapidity and forward-rapidity production of hadrons in polarized p + p collisions at $\sqrt{s} = 200$ and 62.4 GeV, Phys. Rev. D **90**, 012006 (2014).

[27] A. Adare *et al.* (PHENIX Collaboration), Centrality categorization for $R_{p(d)+A}$ in high-energy collisions, Phys. Rev. C **90**, 034902 (2014).

[28] S. S. Adler *et al.* (PHENIX Collaboration), Detailed study of high-p_T neutral pion suppression and azimuthal anisotropy in Au+Au collisions at $\sqrt{s_{NN}} = 200$ GeV, Phys. Rev. C **76**, 034904 (2007).

[29] S. Afanasiev *et al.* (PHENIX Collaboration), High-p_T π^0 production with respect to the reaction plane in Au+Au Collisions at $\sqrt{s_{NN}} = 200$ GeV, Phys. Rev. C **80**, 054907 (2009).

[30] A. Adare *et al.* (PHENIX Collaboration), Neutral pion production with respect to centrality and reaction plane in Au + Au collisions at $\sqrt{s_{NN}} = 200$ GeV, Phys. Rev. C **87**, 034911 (2013).

[31] L. Aphecetche *et al.* (PHENIX Collaboration), PHENIX calorimeter, Nucl. Instrum. Methods Phys. Res., Sect. A **499**, 521 (2003).

[32] G. Aad *et al.* (ATLAS Collaboration), Observation of Long-Range Elliptic Azimuthal Anisotropies in $\sqrt{s} = 13$ and 2.76 TeV pp Collisions with the ATLAS Detector, Phys. Rev. Lett. **116**, 172301 (2016).

[33] V. Khachatryan *et al.* (CMS Collaboration), Pseudorapidity dependence of long-range two-particle correlations in pPb collisions at $\sqrt{s_{NN}} = 5.02$ TeV, Phys. Rev. C **96**, 014915 (2017).

[34] T. A. Trainor and D. T. Kettler, Comparing the same-side ridge in p-p angular correlations at 7 TeV to data measured at the BNL Relativistic Heavy Ion Collider, Phys. Rev. C **84**, 024910 (2011).

[35] B. B. Back *et al.* (PHOBOS Collaboration), Scaling of charged particle production in d+Au collisions at $\sqrt{s_{NN}} = 200$ GeV, Phys. Rev. C **72**, 031901 (2005).

[36] V. Khachatryan *et al.* (CMS Collaboration), Evidence for transverse momentum and pseudorapidity-dependent event plane fluctuations in PbPb and pPb collisions, Phys. Rev. C **92**, 034911 (2015).